Optimizing Yolk–Shell ZnCo$_2$S$_4$ Nanoparticles for Enhanced Supercapacitor Performance: Failure Mechanism Analysis and Material Design

Hsing-I Hsiang,[a] Ming-Hao Chang,[a] and Sheng-Heng Chung*[b, c]

Ternary metal sulfides hold the potential to deliver electrochemical supercapacitors with theoretically high power and energy densities, as well as an extended cycle life. However, the novel bimetallic ternary metal sulfides suffer from rapid loss of their specific capacitance and poor cycle life because their electrochemical reactions involve multiple redox steps, volume expansion, and irreversible structural changes. Thus, understanding the failure mechanisms in terms of the material chemistry is important for designing novel energy materials with high electrochemical stability during long-term cycling. In this study, yolk–shell ZnCo$_2$S$_4$ (ZCS) nanoparticles are synthe- sized and modified with either a carbon shell (ZCS@C) or a polypyrrole (PPy) coating (ZCS@PPy) to explore the failure mechanism of yolk–shell ZCS nanoparticles *via* the decomposition of their shells. The optimal ZCS@C addresses these issues, producing high capacitance (171 F g^{-1} at 2 A g^{-1}) with high retention (78% after 5,000 cycles). Therefore, we comprehensively report this investigation on the effects of the physical chemistry and electrochemistry of ZCS materials on the performance of electrochemical supercapacitors, aiming to design ZCS@C electrochemical materials that effectively address the proposed failure mechanisms.

Introduction

As global electricity demands continually increase with traditional energy sources becoming more limited, investment in new energy industries has surged, leading to greater demands for energy storage technologies, such as supercapacitors and rechargeable batteries. Various supercapacitor devices (*i.e.*, electric double-layer capacitors,[1–3] electrochemical pseudocapacitors,[4,5] and hybrid capacitors[4–6]) offer high levels of safety because they do not rely on chemical reactions.[5–7] These devices can also be charged quickly while providing high power output and maintaining a long cycle life. These properties could allow supercapacitors to synergize with or even replace batteries in certain applications, especially where power density requirements are critical. Unfortunately, although supercapacitors could provide high power densities, faster charge–discharge rates, longer cycle life, and improved stability compared with rechargeable batteries, the low energy density of supercapacitors remains a challenge.[1–3,7] To address this challenge, recent studies have explored new electrode materials with high theoretical charge-storage behavior and reversibility,

such as three-dimensional carbon,[1–3,8] metal oxides,[5,9–11] metal sulfides,[12–15] and polymers.[5–7,16] Moreover, the candidate electrode materials can be modified by novel material morphologies and structures to improve their electrochemical characteristics and performance.[8–16]

Recent studies have focused on adapting pseudocapacitors with high power and energy densities to develop asymmetric supercapacitors, which consist of an electric double-layer capacitor electrode with fast discharging–charging capability and a pseudocapacitor electrode with high electrochemical performance.[4–6] Such pseudocapacitors, based on fast reversible multielectron surface Faradaic redox reactions over electrode materials, can provide larger specific capacitance than electric double-layer capacitors. Extensive research efforts have focused on pseudocapacitors to further improve their performance, which is closely related to the material and electrochemical characteristics of their electrode materials.[4–8] Therefore, the design and synthesis of electrode materials with the required structure and composition have become critical research fields. Fundamental pseudocapacitor electrodes are mainly based on metal oxides, and attention has shifted to metal sulfides characterized by high charge-storage capabilities and electrical conductivities, such as cobalt sulfide (CoS), nickel sulfide (NiS), and molybdenum disulfide (MoS$_2$).[17–20] Studies of transition metal sulfide electrode materials have also demonstrated that the addition of various metal elements can effectively improve these materials' electrical conductivity and accelerate both electron and ion transfer.[20,21] Ternary metal sulfides (*e.g.*, the cobalt sulfides of manganese (MnCo$_2$S$_4$),[22–24] nickel (NiCo$_2$S$_4$),[12,14,25] copper (CuCo$_2$S$_4$),[13,26,27] and zinc (ZnCo$_2$S$_4$))[15,28] have emerged as promising Faradaic electrode materials because of their high catalytic activity, excellent redox reversibility, low electronegativity, and abundant valence states.

[a] Dr. H.-I Hsiang, M.-H. Chang
Department of Resources Engineering, National Cheng Kung University, No. 1, University Road, Tainan City 70101

[b] Dr. S.-H. Chung
Department of Materials Science and Engineering, National Cheng Kung University, No. 1, University Road, Tainan City 70101
E-mail: SHChung@gs.ncku.edu.tw

[c] Dr. S.-H. Chung
Hierarchical Green-Energy Materials Research Center, National Cheng Kung University, No. 1, University Road, Tainan City 70101

Supporting information for this article is available on the WWW under https://doi.org/10.1002/batt.202400403

Batteries & Supercaps

Research Article
doi.org/10.1002/batt.202400403

Chemistry Europe
European Chemical
Societies Publishing

These materials are characterized by the abundant valence states of the added elements, which enhance the materials' conductivity and reduce their energy gap, thereby facilitating the redox reaction for favorable specific electrical properties.[19–21] Besides the improved high capacitance of these materials, research is also needed to improve their cycling rate performance, electrochemical stability, and power/energy densities to further their practical applications. Recent studies of material design and the corresponding structures have proposed that core–shell, yolk–shell, and nano-sphere structures should provide high utilization and stability for the electrode material.[11–17] The modified electrode materials could be further decorated with conductive carbon and polymers as additives or substrates so that electrons could be released and stored in the supercapacitor at a superior rate and efficiency. Moreover, supercapacitor electrodes developed with large specific surface areas and structural durability can compensate for the low energy density.[3–6]

Herein, we explore the electrochemical characteristics of the zinc cobalt sulfide ($ZnCo_2S_4$; ZCS) pseudocapacitor electrode and its failure mechanism. To achieve this, we synthesized two optimal ZCS nanocomposites with either a carbon shell or a conductive polymer coating to extend the cycle life and stability of the ZCS electrode. The ZCS nanoparticle with a yolk–shell nanostructure was first synthesized to enlarge its reaction area and mesoporosity, which could have facilitated the nanoparticle's redox reaction and charge transfer with improved stability.[15] Unfortunately, these changes did not prevent capacitance fade during long-term cycling.[15,28] The failure mechanism was identified as the decomposition of the Co—S bonds in ZCS and the reaction of ZCS with the potassium hydroxide (KOH) electrolyte to form cobalt hydroxide oxide (CoO(OH)) and cobalt(II) hydroxide ($Co(OH)_2$), thus leading to the irreversible loss of the sulfur and active material.[12–15] To address this failure mechanism, we synthesized a carbon-coated ZCS yolk–shell structure (ZCS@C) and a polypyrrole (PPy)-coated ZCS yolk–shell structure (ZCS@PPy), with the conductive protective layer designed to improve the material's charge-transfer capability and structural stability. In an asymmetric supercapacitor, the ZCS@C nanocomposite had high capacitances of 171 F g^{-1} at 2 A g^{-1} and 27 F g^{-1} at 15 A g^{-1}, demonstrating extended long-term stability compared with the ZCS@PPy (with 64 F g^{-1} at 2 A g^{-1} and 21 F g^{-1} at 15 A g^{-1}); this indicates that the ZCS@C design had effectively preserved the Co—S bonds. Moreover, an asymmetric cell with active material designed to couple with ZCS@C demonstrated high capacity retention of 80% after an extended life of 5,000 cycles, compared with 33% for ZCS. Thus, we demonstrate that the explored failure mechanism of ZCS and the resulting poor cycle life can be addressed by the ZCS@C nanocomposite, with the robust carbon protective layer providing long life.

Results and Discussion

In Figure 1a, the X-ray diffraction (XRD) analysis shows that ZCS decomposed and formed $Co(OH)_2$ and CoO(OH) after long-term cycling (Figure S1). To address this issue, ZCS@C and ZCS@PPy were designed with a conductive carbon shell and polymer coating, respectively, to prevent the fast decomposition of the ZCS active material. Comparing these two samples, ZCS@C maintains the crystalline phase of ZCS well, with no impurity phase (Figure S2), while ZCS@PPy does not fully prevent ZCS decomposition (Figure S3). Morphological observations via scanning electron microscopy (SEM) show the shrinkage of the yolk–shell ZCS particles, with an original diameter of 600 nm,
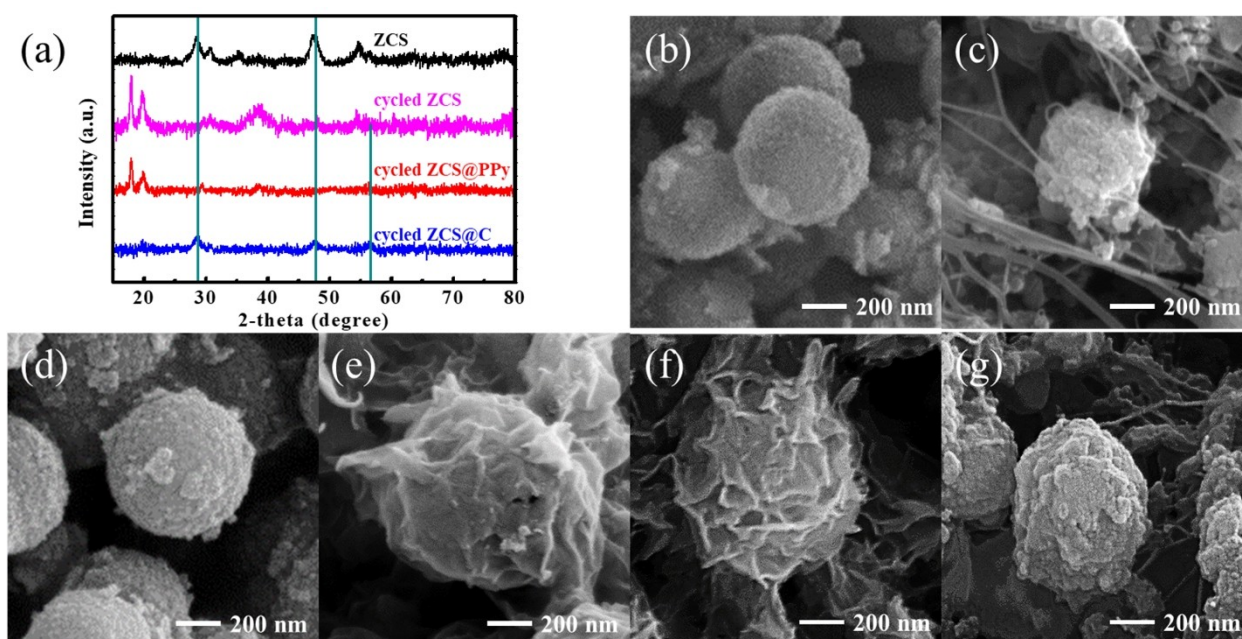

Figure 1. Material and morphological analysis: (a) XRD of ZCS particles; (b–g) SEM of (b, c) ZCS, (d, e) ZCS@C, and (f, g) ZCS@PPy particles (b, d, f) before and (c, e, g) after cycling.

Batteries & Supercaps

Research Article
doi.org/10.1002/batt.202400403

Chemistry Europe
European Chemical
Societies Publishing

and the observable impure byproducts of CoO(OH) and Co(OH)$_2$ (Figure 1b and c, Figures S4 and S5) after 1,200 cycles, which indicate the decomposition of the shell and the exposure of the yolk. However, ZCS@C and ZCS@PPy both avoid the shrinkage of the particles, maintaining the initial particle diameter of 600 nm (Figure 1d–g). This suggests that the carbon shell of ZCS@C protects both the physical structure and chemical composition of the yolk–shell ZCS, whereas ZCS@PPy primarily maintains the physical structure of the coated ZCS, but that its chemical composition still decomposes.[15,28]

In Figure 2, transmission electron microscopy (TEM) reveals the microstructural and crystalline properties of the ZCS active materials. The pristine yolk–shell ZCS initially retains its shell to prolong the stability of the yolk, but the shell decomposes after a long cycle life of 2,000 cycles, exposing the yolk and leading to its rapid deterioration (Figure 2a and b). The corresponding selected-area electron diffraction (SAED) pattern confirms the material decomposition of the yolk–shell ZCS to form Co(OH)$_2$ and CoO(OH) (Figure 2c). In comparison, ZCS@C has a thin carbon shell covering the ZCS (Figure 2d), which stabilizes the physical structure and the chemical composition of ZCS (Figure 2e and f). Interestingly, the PPy coating of ZCS@PPy protects the remaining structure of the ZCS active material while showing impure decomposition products (Figure 2g–i). The above material, morphology, and crystal analyses of the ZCS particles indicate that the yolk–shell structure prolongs the cycle stability of ZCS. However, the robust carbon shell of ZCS@C is needed to protect the ZCS active material for long-term cyclability. By contrast, ZCS@PPy only delays the collapse of the shell, representing a relatively minor improvement in the stability of ZCS.

In Figure 3a–c, the electrochemical cyclic voltammetry (CV) analysis shows the redox reactions of ZnSOH+OH$^-$⇌ZnSO+

H$_2$O+e$^-$ and CoSOH+OH$^-$⇌CoSO+H$_2$O+e$^-$.[12,22–28] As the scan rate increases, ZCS and ZCS@PPy show increases in the cell polarization caused by the incurred resistance. However, ZCS@C shows an enlarged CV area and almost overlapping CV peaks, indicating its enhanced electrochemical utilization and accelerated charge transfer (Figure 3b). Galvanostatic charge–discharge (GCD) analysis shows that the specific capacitances of ZCS, ZCS@C, and ZCS@PPy reach 1,262, 1,196, and 1,025 F g^{-1} at 2 A g^{-1}, and remain at 1,166, 1,160, and 762 F g^{-1} at 15 A g^{-1}, respectively (Figure 3d–f). This results in corresponding rate capacities of 92%, 96%, and 74%, and indicates that adding a conductive carbon shell improves the high rate performance of ZCS, whereas adding a polymer coating might inhibit the high rate functionality of ZCS. Similarly, Figure 3g shows that the capacitance loss of ZCS at high current density can be resolved by the carbon shell. However, the polymer coating might block the charge transfer pathway, resulting in the relatively low capacitance and rate performance of ZCS@PPy. Moreover, the cycle stability of ZCS shows capacitance retention of 65%, 71%, and 63% for ZCS, ZCS@C, and ZCS@PPy after 1,200 cycles at 15 A g^{-1}, respectively (Figure 3h). This further demonstrates the high-rate operational stability and performance of ZCS@C

In Figure 4, the ZCS particles are tested via electrochemical performance analysis in an asymmetric cell with activated carbon as the negative electrode and the resulting ZCS particles as the positive electrolyte in a regular 3 M battery electrolyte. In Figure 4a–c, the CV analysis demonstrates typical asymmetric supercapacitance behavior, with a rectangular shape indicating the double-layer reaction and anodic–cathodic peaks representing the Faradaic reaction during charging and discharging. The double-layer capacitance results from the activated-carbon negative electrode, while the indistinct peaks are attributable to Faradaic reactions related to zinc hydroxysulfide (ZnSOH) and
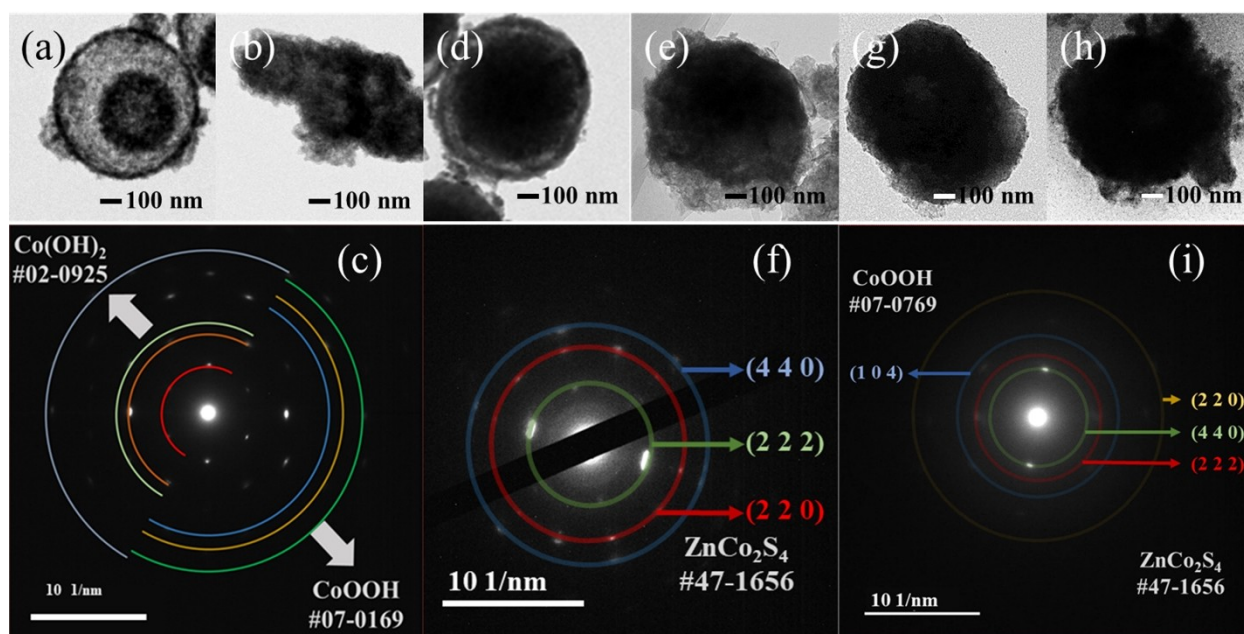

Figure 2. Microstructural and crystal analysis: (a, b, d, e, g, h) TEM and (c, f, i) SAED of (a, b) ZCS, (d, e) ZCS@C, and (g, h) ZCS@PPy particles (a, d, g) before and (b, e, h) after cycling.
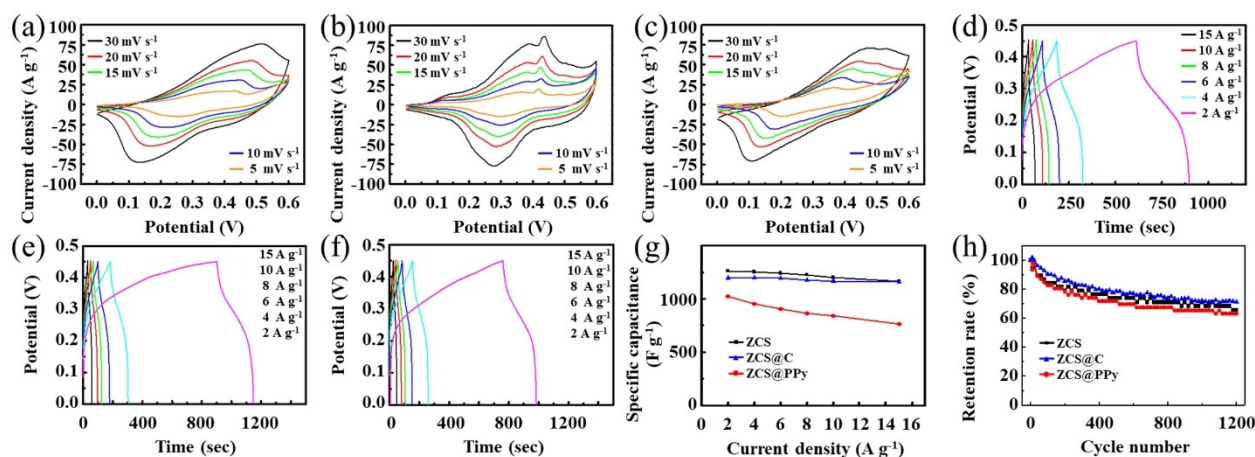
Figure 3. Electrochemical analysis of ZCS active materials: (a–c) CV of (a) ZCS, (b) ZCS@C, and (c) ZCS@PPy at 5–30 mV s^{-1}; (d–f) GCD of (d) ZCS, (e) ZCS@C, and (f) ZCS@PPy at 2–15 A g^{-1}; (g) rate performance at 2–15 A g^{-1}; and (h) capacitance retention at 15 A g^{-1}.
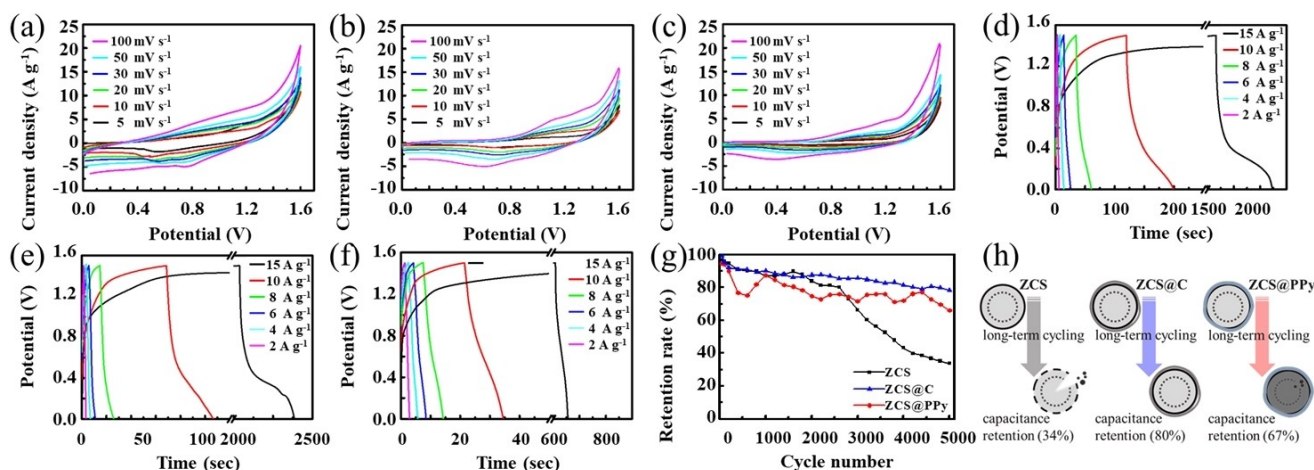

Figure 4. Asymmetric supercapacitor properties: (a–c) CV of (a) ZCS, (b) ZCS@C, and (c) ZCS@PPy at 5–100 mV S^{-1}; (d–e) GCD of (d) ZCS, (e) ZCS@C, and (f) ZCS@PPy at 2–15 A g^{-1}; (g) capacitance retention at 15 A g^{-1}; and (h) failure mechanism and optimization design.

cobalt hydroxysulfide (CoSOH).[12,22–28] Varying the scan rate does not obviously change the CV curves and peaks of the cells, indicating that the yolk–shell ZCS structure contributes to stabilizing the electrochemical performance. However, using ZCS@PPy leads to a relatively low CV performance. In Figure 4d–f, the GCD profiles further examine the stability and rate performance of the cell with different ZCS particles. The cells using ZCS, ZCS@C, and ZCS@PPy demonstrate specific capacitances of 128, 171, and 64 F g^{-1} at 2 A g^{-1}, and remain at 14, 27, and 21 F g^{-1} at 15 A g^{-1}, respectively. This results in corresponding rate capacities of 11 %, 16 %, and 32 %, indicating that the conductive carbon shell of ZCS@C has improved its utilization and retention during high-rate operation. Therefore, the high energy and power densities of 40 Wh kg^{-1} and 1500 W kg^{-1} for ZCS are enhanced to 54 Wh kg^{-1} and 1500 W kg^{-1} for ZCS@C, while they decrease to 20 Wh kg^{-1} and 1500 W kg^{-1} for ZCS@PPy. In Figure 4g, the cycle stability of the supercapacitor cells are examined at 15 A g^{-1}. With the yolk–shell ZCS

providing the active materials, the cells show good cycle stability over the initial 2,000 cycles. After that, the reference ZCS starts to exhibit capacitance fading, resulting in a low capacitance retention of 33 %, with 50 % capacitance loss shown during the long-term cycling from 3,000–5,000 cycles. ZCS@C and ZCS@PPy, designed to resolve these problems, both show enhanced capacitance retention of 78 % and 66 % after 5,000 cycles, respectively, demonstrating the superior capacitance stability of the ZCS@C. The electrochemical impedance analysis of the cells before and after cycling reveals that ZCS@C and ZCS@PPy exhibit improved electronic conductivity due to the application of the electron-transfer coating (Figure S6). This coating slightly mitigates the direct contact between the ZCS electrode material and the KOH electrolyte. Despite an increase in diffusion impedance, the cycled cells with the conductive shell protecting the ZCS material maintain low resistance. Among them, ZCS@C exhibits lower resistance compared to ZCS@PPy, aligning with material analysis, which indicates that

Batteries & Supercaps

Research Article
doi.org/10.1002/batt.202400403

Chemistry Europe
European Chemical
Societies Publishing

the conductive carbon shell effectively stabilizes both the configuration and composition of ZCS.[27–29]

The failure mechanism of the yolk–shell ZCS materials (*i.e.*, ZCS, ZCS@C, and ZCS@PPy) during long-term operation is expounded in Figure 4 h, based on the material and electrochemical analyses presented above. Material analysis of the cycled ZCS sample reveals a two-stage reaction in the yolk–shell-structured ZCS active material. In the first stage, the yolk–shell ZCS retains its shell to inhibit the fast decomposition of ZCS material and KOH electrolyte. However, over the long-term cycling of the second stage, the ZCS shell is consumed and decomposed into the reaction byproducts, CoO(OH) and Co-(OH)$_2$, resulting in ZCS losing a large amount of sulfur and reducing its long-term stability.[22–28] This two-step material reaction accounts for the high stability during the first 2,000 cycles and the subsequent fast capacitance fading of the yolk–shell ZCS electrode. Therefore, this suggests that shell stabilization should improve the long-term operational stability of the yolk–shell ZCS. We achieved this stabilization for both ZCS@C and ZCS@PPy by applying conductive carbon and polymer coatings, respectively, at the interface between the ZCS electrode material and the KOH electrolyte to slow shown the decomposition of ZCS's structure and composition. Material and structural analyses reveal that these coatings effectively preserve the integrity and surface layer of the 600-nm-diameter yolk–shell ZCS particles during long-term cycling. Crystal and phase analyses also reveal that ZCS@C maintains the chemical stability of ZCS and reduces sulfur loss. In contrast, while ZCS@PPy preserves particle morphology, it does not stabilize ZCS under the PPy coating, leading to ZCS decomposition. The decomposed ZCS@PPy shows the presence of a PPy shell and CoO(OH) byproducts, resulting in a relatively low sulfur content in the electrode material. In summary, ZCS@C protects ZCS with its carbon shell, enabling the stabilized ZCS to achieve high and consistent electrochemical performance.

Conclusions

In conclusion, we investigated the failure mechanism of yolk–shell ZCS during its long-term cycling, demonstrating that the decomposition of the ZCS shell causes the material to lose its protective layer. This results in the loss of sulfur and the formation of CoO(OH) and Co(OH)$_2$, which represent the irreversible loss of the ZCS active material in terms of both its configuration and chemical composition. However, an additional carbon shell can strengthen the protective shell of ZCS. This ZCS@C nanocomposite protects the ZCS shell, stabilizing the morphology and composition of the active material, while also attaining high energy and power densities with long cycle life with improved capacity retention.

Experimental

Synthesis of yolk–shell zinc cobalt sulfide (ZnCo$_2$S$_4$; ZCS), carbon-coated yolk–shell ZnCo$_2$S$_4$ (ZCS@C), and polypyrrole (PPy)-coated

yolk–shell ZnCo$_2$S$_4$ (ZCS@PPy) nanoparticles: The yolk–shell ZCS nanoparticles were prepared based on our previous research under the optimal conditions for the two-step hydrothermal synthesis method. First, 0.1488 g of zinc nitrate hexahydrate (Zn(NO$_3$)$_2$·6H$_2$O, 99%, J.T.Baker), 0.2912 g of cobalt(II) nitrate hexahydrate (Co-(NO$_3$)$_2$·6H$_2$O, 99%, Acros), 15 mL of glycerol (C$_3$H$_5$(OH)$_3$, 99.5%, anhydrous, J.T.Baker), and 105 mL of isopropanol ((CH$_3$)$_2$CHOH, 99.5%, Duksan) were uniformly mixed. The mixture was then heated to 180 °C for 24 h in a cylindrical polytetrafluoroethylene (PTFE)-sealed autoclave, allowing Zn(NO$_3$)$_2$·6H$_2$O and Co-(NO$_3$)$_2$·6H$_2$O to react with glycerol ligands and form a zinc–cobalt–glycerate precursor, consists of Co(C$_3$H$_5$O$_4$)$_2$ and Zn(C$_3$H$_5$O$_4$)$_2$ complexes.[15,29–31] The resulting purple powder, the zinc–cobalt–glycerate precursor, was rinsed with ethanol and dried in an air-flow oven for 24 h. Then, in the second step of material synthesis, 0.18 g of the as-prepared zinc–cobalt–glycerate precursor, 0.3 g of thioacetamide (C$_2$H$_5$NS, 98%, Alfa Aesar), and 120 mL of ethanol (C$_2$H$_5$OH, 99.5%, Nihon Shiyaku) were mixed, then transferred to a PTFE-sealed autoclave at 200 °C for 18 h. This process allowed the glycerol ligands in the cobalt and zinc precursors to be replaced by sulfide anions. This ligand replacement facilitated the synthesis of ZCS, characterized by cobalt in the 3+ oxidation state,[15,30,32–36] and the varying diffusion rates of anions, resulting in a yolk–shell nanoparticle configuration.[15,32–36] The ZCS@C nanoparticles were synthesized from the same zinc–cobalt–glycerate precursor, with the addition of 0.36 g of glucose (C$_6$H$_{12}$O$_6$, 99.5%, J.T.Baker) as the carbon source, and 0.035 g of L-ascorbic acid (C$_6$H$_8$O$_6$, 99%, Sigma-Aldrich) as both a carbon source and a charge transfer complex. These components facilitated the formation of a carbon shell around the ZCS nanoparticles during the heat treatment process, forming the ZCS@C nanoparticles.[37] The ZCS@PPy was also synthesized from the zinc–cobalt–glycerate precursor, forming ZCS as a working electrode with 0.1 M 2,6-naphthalene-disulfonic acid disodium salt (C$_{10}$H$_6$(SO$_3$Na)$_2$, 97%, Sigma-Aldrich) and 0.1 M pyrrole monomer mixtures as the reaction solution. After two cyclic voltammetry (CV) scans between −0.2 V and 1.02 V at 100 mV s^{-1}, the ZCS@PPy nanoparticles were obtained.

Material characterization: Material identification was conducted using X-ray diffraction (XRD; D8 Discover with GADDS, Bruker) with a copper target (CuKα = 1.5406 Å) at an operating voltage and current of 40 kV and 40 mA, respectively. The material identification data were collected from $2\theta = 15°$ to 80°. The morphological observation was conducted by scanning electron microscopy (SEM; SU1510, Hitachi). The microstructural and crystal analysis was conducted by high-resolution transmission electron microscopy (HR-TEM; JEM-2100F, JEOL; and TEM; JEM-2010, JEOL).

Electrochemical characterization: Electrochemical characterization of the active materials was conducted in a three-electrode electrochemical test station with the active-material working electrode, a mercury–mercury oxide (Hg–HgO) reference electrode, and a platinum counter electrode immersed in 3 M potassium hydroxide (KOH) electrolyte. Electrochemical measurements were conducted using a potentiostat/galvanostat and an electrochemical interface for a frequency response analyzer (1287/1260 Solarton). The active-material working electrodes with ZCS, ZCS@C, or ZCS@PPy were prepared by mixing the active material (*i.e.*, ZCS, ZCS@C, and ZCS@PPy), carbon black, and PTFE in a weight ratio of 85 : 10 : 5 to form the active-material paste. Then, 60 μL of the as-prepared paste was drop-cast onto a nickel-foam current collector (1.5 cm×1 cm) with a fixed coating area of 1 cm^2 as the working electrode after drying at 80 °C for 24 h. The asymmetric supercapacitor properties of the active materials were analyzed with ZCS, ZCS@C, or ZCS@PPy as the positive electrode and activated carbon as the negative electrode in a cell with a glass-fiber separator and 3 M KOH electrolyte. The mass ratio of the ZCS, ZCS@C, and ZCS@PPy

Batteries & Supercaps

Research Article
doi.org/10.1002/batt.202400403

Chemistry
Europe
European Chemical
Societies Publishing

positive electrodes and the activated-carbon negative electrode was $1:10$ based on the equation: $m_{(positive)} \times C_{(positive)} \times \triangle V_{(positive)} = m_{(negative)} \times C_{(negative)} \times \triangle V_{(negative)}$, where m is the mass of the electrode, C is the specific capacitance of the electrode, and $\triangle V$ is the operational voltage window of the electrode. CV measurements of ZCS, ZCS@C, and ZCS@PPy materials were performed at 0.0–0.6 V (vs. Hg/HgO) with scan rates of 5, 10, 15, 20, and $30\,\mathrm{mV\,s^{-1}}$. The corresponding CV analysis of the resulting positive electrodes in the asymmetric supercapacitor was conducted at 0.0–1.6 V with scan rates of 5, 10, 20, 30, 50, and $100\,\mathrm{mV\,s^{-1}}$. Galvanostatic charge–discharge (GCD) analysis of ZCS, ZCS@C, and ZCS@PPy materials was performed at 0.0–0.45 V (vs. Hg/HgO) and the resulting positive electrodes in the asymmetric supercapacitor were tested at 0.0–1.5 V with current densities of 2, 4, 6, 8, 10, and $15\,\mathrm{A\,g^{-1}}$. The cyclability was measured for 1,200 cycles for the ZCS, ZCS@C, and ZCS@PPy materials and for 5,000 cycles for the corresponding asymmetric supercapacitor. The specific capacitance ($C\,[\mathrm{F\,g^{-1}}] = (i \times \triangle t)/(m \times \triangle V)$), energy density ($E\,[\mathrm{Wh\,kg^{-1}}] = (C \times \triangle V^2)/2$), and power density ($P\,[\mathrm{W\,kg^{-1}}] = E/\triangle t$) were calculated, where i (A) is the discharge current, $\triangle t$ (s) is the discharge period, m (g) is the mass of the active material, and $\triangle V$ (V) is the operating voltage window of the electrode. Electrochemical impedance analysis was performed with an AC amplitude of 5 mV and a frequency range from 0.1 Hz to 10 MHz on the cells containing ZCS, ZCS@C, and ZCS@PPy, both before and after cycling.

Supporting Information Summary

Supporting Figures S1–S6: material and electrochemical analyses of ZCSs; Supporting Tables S1 and S2: material analysis of ZCSs.

Acknowledgements

Conflict of Interests

The authors declare no conflict of interest.

Data Availability Statement

The data that support the findings of this study are available from the corresponding author upon reasonable request.

[1] C. Schütter, S. Pohlmann, A. Balducci, *Adv. Energy Mater.* **2019**, *9*, 1900334.
[2] M. E. Şahin, F. Blaabjerg, A. Sangwongwanich, *Energy* **2022**, *15*, 674.
[3] J. Wu, *Chem. Rev.* **2022**, *122*, 10821–10859.
[4] Y. Jiang, J. Liu, *Energy Environ. Mater.* **2019**, *2*, 30–37.
[5] P. Bhojane, *J. Energy Storage* **2022**, *45*, 103654.
[6] D. P. Chatterjee, A. K. Nandi, *J. Mater. Chem. A* **2021**, *9*, 15880–15918.
[7] M. Winter, R. J. Brodd, *Chem. Rev.* **2004**, *104*, 4245–4270.
[8] Z. Zhai, L. Zhang, T. Du, B. Ren, Y. Xu, S. Wang, J. Miao, Z. Liu, *Mater. Des.* **2022**, *221*, 111017.
[9] H. Chen, J. Wang, X. Han, F. Liao, Y. Zhang, L. Gao, C. Xu, *Ceram. Int.* **2019**, *45*, 8577–8584.
[10] Y. Gao, Y. Xia, H. Wan, X. Xu, S. Jiang, *Electrochim. Acta* **2019**, *301*, 294–303.
[11] X. Liu, F. Wei, Y. Sui, J. Qi, Y. He, Q. Meng, *J. Alloys Compd.* **2018**, *735*, 1339–1343.
[12] L. Liu, T. Chen, H. Rong, Z. Wang, *J. Alloys Compd.* **2018**, *766*, 149–156.
[13] H. Li, Z. Li, Z. Wu, M. Sun, S. Han, C. Cai, W. Shen, X. T. Liu, Y. Fu, *J. Colloid Interface Sci.* **2019**, *549*, 105–113.
[14] H.-I. Hsiang, C.-H. She, S.-H. Chung, *Ceram. Int.* **2021**, *47*, 25942–25950.
[15] H.-I. Hsiang, Y.-Y. Chiou, S.-H. Chung, *J. Energy Storage* **2022**, *55*, 105402.
[16] J. A. Oke, T.-C. Jen, *J. Mater. Res. Technol.* **2022**, *21*, 2481–2514.
[17] F. Lu, M. Zhou, W. Li, Q. Weng, C. Li, Y. Xue, X. Jiang, X. Zeng, Y. Bando, D. Golberg, *Nano Energy* **2016**, *26*, 313–323.
[18] X. Y. Yu, X. W. Lou, *Adv. Energy Mater.* **2018**, *8*, 1701592.
[19] X. Y. Yu, L. Yu, X. W. Lou, *Adv. Energy Mater.* **2016**, *6*, 1501333.
[20] P. Geng, S. Zheng, H. Tang, R. Zhu, L. Zhang, S. Cao, H. Xue, H. Pang, *Adv. Energy Mater.* **2018**, *8*, 1703259.
[21] B. Y. Guan, L. Yu, X. Wang, S. Song, X. W. Lou, *Adv. Mater.* **2017**, *29*, 1605051.
[22] J. Yang, M. Ma, C. Sun, Y. Zhang, W. Huang, X. Dong, *J. Mater. Chem. A* **2015**, *3*, 1258–1264.
[23] R. Li, S. Wang, Z. Huang, F. Lu, T. He, *J. Power Sources* **2016**, *312*, 156–164.
[24] A. González, E. Goikolea, J. A. Barrena, R. Mysyk, *Renewable Sustainable Energy Rev.* **2016**, *58*, 1189–1206.
[25] L. Shen, L. Yu, H. B. Wu, X.-Y. Yu, X. Zhang, X. W. Lou, *Nat. Commun.* **2015**, *6*, 6694.
[26] J. Tang, Y. Ge, J. Shen, M. Ye, *Chem. Commun.* **2016**, *52*, 1509–1512.
[27] N. Tang, H. You, M. Li, G. Z. Chen, L. Zhang, *Nanoscale* **2018**, *10*, 20526–20532.
[28] Y. M. Cheng, Z. Li, X. W. Lou, *Angew. Chem. Int. Ed.* **2015**, *54*, 10521–10524.
[29] Z. Dong, W. Zhang, Y. Xiao, Y. Wang, C. Luan, C. Qin, Y. Dong, M. Li, X. Dai, X. Zhang, *ACS Sustainable Chem. Eng.* **2020**, *8*, 5464–5477.
[30] L. Shen, L. Yu, X.-Y. Yu, X. Zhang, X. W. Lou, *Angew. Chem. Int. Ed.* **2015**, *54*, 1868–1872.
[31] H. Liu, Y. Liu, X. Sheng, M. Zhang, S. Tan, X. Zhao, L. Zheng, *Mater. Lett.* **2024**, *357*, 135683.
[32] M. Zhu, J. Tang, W. Wei, S. Li, *Mater. Chem. Front.* **2020**, *4*, 1105–1149.
[33] M. Zhu, Y. Cheng, Q. Luo, M. El-khateeb, Q. Zhang, *Mater. Chem. Front.* **2021**, *5*, 2552–2587.
[34] Q. Luo, C. Lu, L. Liu, M. Zhu, *Microstructures* **2023**, *3*, 2023011.
[35] M. Zhu, X. Li, C. Tu, Q. Luo, Y. Nie, J. Pan, S. Li, *Mater. Chem. Front.* **2022**, *6*, 203–212.
[36] M. Zhu, Q. Luo, C. Lu, L. Liu, *Appl. Organomet. Chem.* **2024**, *38*, e7354.
[37] T. Ding, Y. Li, X. Xu, Z. Li, H. Jiao, P. Na, Y. Ding, X. Wang, *Chem. Phys. Lett.* **2023**, *826*, 140645.